Article

Manipulation of lithium dendrites based on electric field relaxation enabling safe and long-life lithium-ion batteries

Xuebing Han[1,6] ✉, Shuoyuan Mao [1,6] ✉, Yu Wang[1,2] ✉, Yao Lu [3], Depeng Wang[4], Yukun Sun[4], Yuejiu Zheng[5] ✉, Xuning Feng[1], Languang Lu[1], Jianfeng Hua[4] & Minggao Ouyang [1] ✉

Lithium dendrites, with their high reactivity, pose a critical challenge to the safety and longevity of lithium-based batteries. Effective regulation strategies are crucial for mitigating battery degradation and enhancing reliability. Conventional approaches, such as relaxation following lithium plating or regulated discharging, often fail to simultaneously address the formation of solid electrolyte interface and isolated lithium. Here, we demonstrate that rational utilization of electric field relaxation following dendrite growth can reduce defective solid electrolyte interface and isolated lithium by balancing solid electrolyte interface growth and dendrite morphology smoothing near the relaxation time constant. Building upon the mechanism, we propose a short-term relaxation method to manipulate lithium plating, which achieves an enhancement of capacity retention from 80% up to 95% at 3 C-rate (20 min) fast-charging on commercial batteries. These findings highlight the importance of relaxation after dendrites formation for safe, long-life and fast-charging batteries, particularly where dendrite growth is the limiting factor.

With their superior energy density and durability, lithium-based batteries have emerged as the cornerstone of energy storage in the pursuit of carbon neutrality[1–3]. However, the growth of lithium dendrites has become a predominant impediment in the application of lithium-based batteries, due to the large surface area and high reactivity between the dendrites and surrounding electrolyte[4–7]. Rapid side reactions of the plated lithium dendrites lead to substantial heat generation and irreversible loss of active lithium, compromising the safe and prolonged operation of the batteries[8–10]. More seriously, during cycling after lithium plating, some lithium dendrites lose electrical contact with the negative electrode and become dead lithium, which further accelerates battery degradation. Therefore,

manipulation strategies for lithium plating are essential for the long-life operation of lithium-ion batteries.

The introduction of functional materials presents an effective approach for post-lithium plating treatment. By ingeniously introducing certain redox pairs, dead lithium can be oxidized and dissolved at specific voltages, thereby recovering into active lithium and significantly extending the battery's lifespan. Recent studies have shown that I^{3-}/I^{-}[11] and Br^{3-}/Br^{-}[12] are two promising redox pairs. However, these approaches involve material modification thus are difficult to be directly applied to existing battery systems.

Based on the understanding of the physical and chemical transformations following lithium plating, the post-lithium plating work

[1]State Key Laboratory of Intelligent Green Vehicle and Mobility, School of Vehicle and Mobility, Tsinghua University, Beijing 100084, China. [2]Beijing Key Laboratory of Green Chemical Reaction Engineering and Technology, Department of Chemical Engineering, Tsinghua University, Beijing 100084, China. [3]Beijing Institute of Nanoenergy and Nanosystems, Chinese Academy of Sciences, Beijing 101400, P. R. China. [4]Sichuan New Energy Vehicle Innovation Center Co., Ltd., Yibin, Sichuan 644005, China. [5]School of Mechanical Engineering, University of Shanghai for Science and Technology, Shanghai 200093, China. [6]These authors contributed equally: Xuebing Han, Shuoyuan Mao. ✉e-mail: hanxuebing@tsinghua.edu.cn; maosy21@mails.tsinghua.edu.cn; lucywang@mail.tsinghua.edu.cn; yuejiu_zheng@163.com; ouymg@tsinghua.edu.cn

protocols have shown significant impact on capacity recovery of lithium-ion batteries. Calendar studies have shown that directly relaxation after lithium dendrites growth leads to the formation of a fragile solid electrolyte interphase (SEI), thus accelerating battery degradation[13–15]. Therefore, in traditional perceptions, the optimal approach after lithium plating is considered to be immediate discharging, which can suppress SEI growth and promote the majority of Li$^+$ to reversibly strip back to cycling. However, the stripping of Li$^+$ leads to the fracture of lithium dendrites, causing the generation of dead lithium thus decreasing the battery capacity retention[11,16–18]. To address these challenges, the state-of-the-art researches have shown that continuous discharging process[15,19–21], pulse current conditions[22–26] and relaxation at the discharged state after lithium plating[27] can partially reactive isolated lithium, which result in over 100% Coulomb Efficiency (CE) in the subsequent cycles, enabling the recovery of capacity loss, as illustrated in Fig. 1a. These approaches shed light on restoring battery performance after lithium plating, however, they are still primarily remedial measures taken after the formation of dead lithium. The regulation approaches to simultaneously suppress undesirable SEI growth and dead lithium formation from the source remain unexplored.

In this study, we find a counterintuitive phenomenon: short-term relaxation (near the time constant of the electric field relaxation process) after lithium plating exhibits the highest capacity retention rate among various parameter combinations of lithium plating-resting-discharging-resting cycles. To figure out the underlying mechanisms, we investigate the chemical and physical changes of lithium dendrites during relaxation after lithium plating. By utilizing in-situ Raman-optical microscopy-electrochemical impedance spectroscopy (EIS) techniques, we find that chemically, the SEI formed in the short term after lithium plating is predominantly inorganic, which is typically considered to be dense and beneficial, whereas prolonged relaxation leads to a significant increase in the loose and adverse organic components; and physically, a decrease in the area covered by lithium dendrites during short-term relaxation after lithium plating occurs, which indicates morphological changes.

Furthermore, by ex-situ X-ray photoelectron spectroscopy (XPS), transmission electron microscope (TEM), scanning electron microscopy (SEM) and energy dispersive spectroscopy (EDS) techniques, the temporal and special formation of SEI after lithium plating is analyzed, and the inorganic-organic staged growth mechanism is confirmed. Then by phase-field modeling, we reveal that during relaxation, the concentration gradient of Li$^+$ shifts from the dendrite tips to the sides, which leads to the gradual smoothing and thickening of the dendrite tips. The fundamental mechanism of both the transformations lies in the localized electric field relaxation during resting after lithium dendrites formation.

Based on the mechanism, we propose a short-term resting manipulation strategy for recovering the lithium dendrite-formed batteries, and validate this approach on commercial 0.9 Ah Graphite (Gr)||lithium iron phosphate (LFP) batteries, which achieves a leap in capacity retention from 80% to 95% over 100 cycles at 3 C (C is the unit of charge rate, 1 C represents the equivalent current that can fully charge the battery in one hour, and 3 C means the current that can fully charge a battery in 20 minutes. For the pouch cell employed, 3 C represents the current of 2.7 A) fast charging. Moreover, compares to the state-of-the-art discharging-resting management technique, our lithium plating manipulation method achieves an 80% reduction in protocol time, and decreases the capacity loss rate by 23.8%. Unexpectedly, we find that the capacity degradation of the full battery is unrelated to CE. The discharging-resting batteries remain above 100% CE for the majority of the time, however, their capacity retention is inferior to the batteries using our proposed regulation protocol, which generally exhibits CE below 100%.

From this study, we suggest that rational utilization of electric field relaxation directly after dendrites formation is a practical manipulation approach for safe, long-life and fast-charging lithium-ion batteries. This study also sheds light on the sustainable manipulation of batteries where dendrite growth is the limiting factor for charging, such as sodium-ion batteries and zinc-ion batteries.

Results

Comparison of post-lithium plating manipulation processes

Zhang et al. investigated the electrochemical and morphological changes during a 10-hour relaxation period at discharged state after lithium plating, and discovered the reactivation of isolated lithium[27]. Here, to comprehensively investigate the impact of different conditions on battery capacity recovery after lithium plating on Gr negative electrodes, we designed a set of test conditions for comparison using Li||Gr cells, as shown in Fig. 1b and Supplementary Table 1. All of the tests were conducted under a 10-hour manipulation period, including resting a hours immediately after lithium plating, followed by discharging and resting for b hours ($a + b = 10$ and $a = 0, 1, 2, 5, 10$). Since it is widely accepted that low-rate plating leads to a more even dendritic morphology, and low-rate stripping helps to avoid dendrite fracture, both methods are anticipated to result in higher capacity retention[28,29], we set up control groups for low-rate plating and low-rate stripping, without resting and with a total time increment of 10 hours, to determine the effectiveness of the manipulation protocols. Then we compared the capacity recovery rates (equal to CE, and shown in Eq. (1)) of the lithium plating-discharging processes under different conditions. To account for the impact of isolated lithium recovery on the CE in the subsequent cycles after lithium plating and striping, we added a normal charging-discharging cycle following the lithium plating-discharging cycle, and then compared the total capacity retention over the two cycles (Eq. (2)), which represents the overall impact of manipulation protocols on capacity recovery.

$$CE = CRR_1 = \frac{Q_{dch,1}}{Q_{ch,1}} \times 100\% \tag{1}$$

$$CRR_2 = \frac{Q_{dch,1} + Q_{dch,2}}{Q_{ch,1} + Q_{ch,2}} \times 100\% \tag{2}$$

In Eqs. (1–2), CE is Coulomb Efficiency, CRR_1 is the capacity retention rate of the lithium plating-discharging process, CRR_2 is the total capacity retention rate over the two cycles, $Q_{ch,1}$ and $Q_{dch,1}$ represents the charge and discharge capacity of the lithium plating-discharging cycle (in Ah), and $Q_{ch,2}$, $Q_{dch,2}$ represents the charge and discharge capacity of the following normal cycle (in Ah).

The comparison results are shown in Fig. 1c. The discharging-resting group ($a = 0$, $b = 10$), low-rate charging and low-rate discharging control groups showed no significant differences, indicating that resting after discharging could restore the capacity after the inadvertent plating of lithium, through the reactivation of isolated lithium. And the discharging-resting group exhibited higher CE compared to the long-term resting groups after lithium plating ($a = 5$, $b = 5$ and $a = 10$, $b = 0$), which was attributed to the extensive SEI growth during resting directly after lithium plating[30]. Thus, the discharging-resting process is more effective for capacity recovery than the long-term resting after plating.

Unexpectedly, the capacity recovery of the short-term relaxation after plating groups ($a = 1$, $b = 9$ and $a = 2$, $b = 8$), whether in the single plating cycle or total two cycles, were significantly higher than other groups. This challenged the conventional belief that relaxation after lithium dendrites formation would lead to abnormal SEI growth and
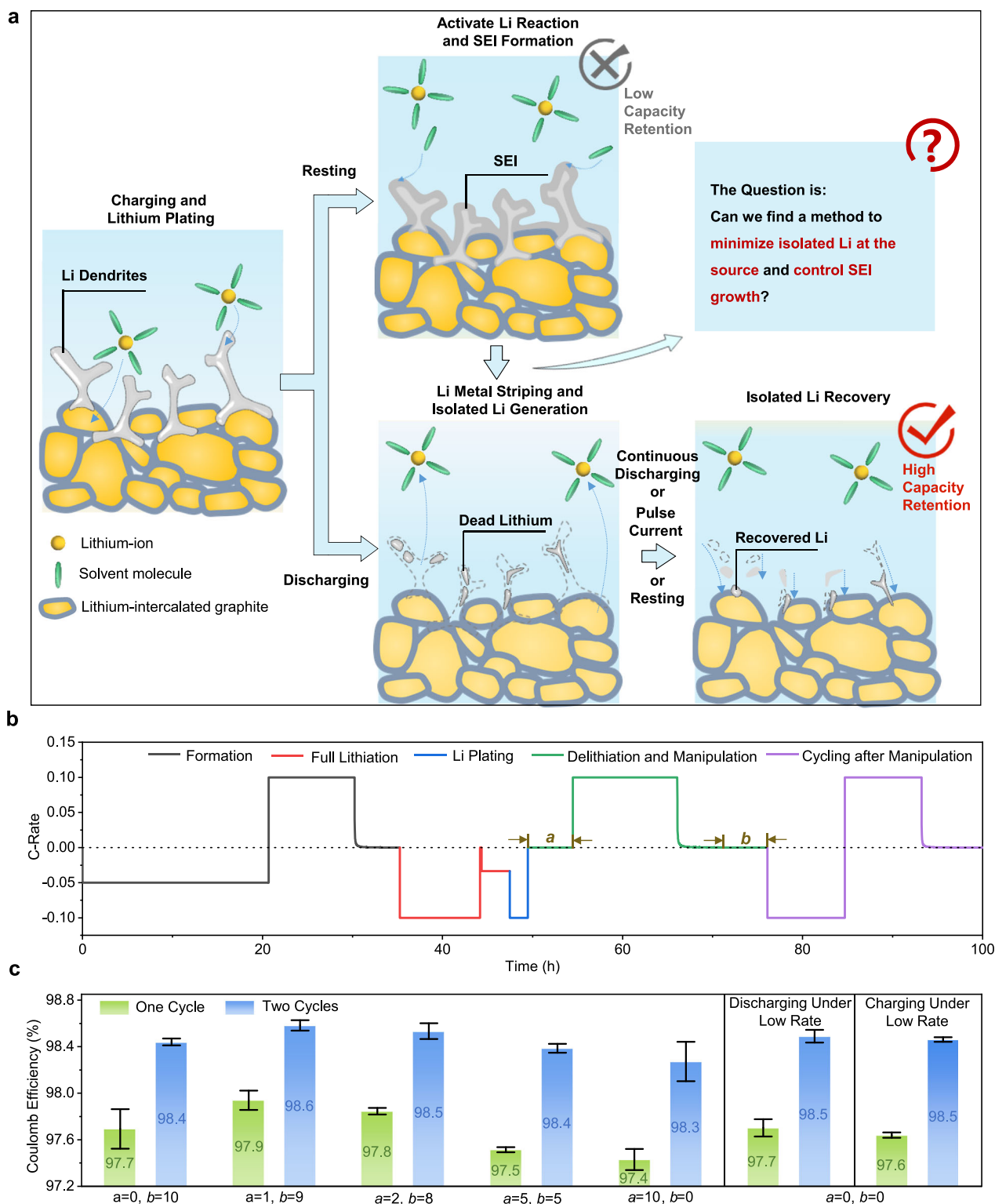
Fig. 1 | The manipulation processes after lithium dendrite plating. a Schematic illustration of reactions after lithium plating at different regulations in conventional understanding. **b** Test protocols. 1 C-rate represents testing under 2.2 mA. **c** The single-cycle and two-cycle capacity retention rates (CRR) under different manipulation processes.

accelerated capacity decay, and indicated a strategy with greater potential to reduce manipulation time, more closely aligning with real-world conditions of short-term relaxation after fast charging. The underlying mechanism during relaxation process subsequent to lithium plating requires in-depth investigation for the reliable operation of batteries.

In-situ observation of the relaxation period after lithium plating

We first designed an in-situ Raman-optical microscopy-EIS setup, to study the structural and chemical changes occurring in the Gr negative electrode with lithium dendrites during the relaxation period after lithium plating, as shown in Supplementary Fig. 1. We refined the design and fabrication process of the optical coin cell[27], making it

convenient for access in normal laboratories (Supplementary Fig. 2-3). The test procedure is shown in Supplementary Fig. 4. Firstly, the Gr negative electrode in the optical cell was charged at 1/20 C (0.12 mA) to generate a robust SEI and fully lithiated Gr (LiC_6)[31]. Secondly, the Gr negative electrode was overcharged at 1 mA for 2 h to induce lithium plating, and finally the cell was rested for 20 h.

Chemically, we analyzed the in-situ Raman test results of the total process, as shown in Fig. 2a. During the lithium plating process, the peak around $500\ cm^{-1}$ associated with Li_2O, and the peak around $1522\ cm^{-1}$ corresponding to ROCOOLi[32-36] both weakened or even disappeared, indicating the plated lithium disrupted the original SEI structure. During the relaxation period after plating, the Li_2O slightly increased within 1-3 hours, followed by a decrease over the long term, while the ROCOOLi significantly increased. This suggests that the SEI regenerated during short-term relaxation was predominantly inorganic (generally considered dense, robust, and of high lifespan performance[37,38]), whereas after long-term relaxation became mainly organic, agreeing with the reported findings (typically regarded as porous and less durable[39,40]).

Physically, we tracked the morphological changes throughout the entire formation-lithium plating-relaxation process, and distinguished the gray metallic lithium from the negative electrode (golden LiC_6 and purplish-red copper mesh) by decomposing the images into RGB color channels[27]. Then we analyzed the lithium plating regions at 0, 0.5, 1 and 5 hours after plating (original images shown in Supplementary Fig. 5). By comparing and subtracting the regions at adjacent time points, we

visualized the changes in lithium plating morphology, as shown in Fig. 2b. It was observed that in early stages of relaxation after plating, the areas covered by metallic lithium gradually diminished, which gradually became less noticeable over time. Further, the semi-quantitative comparison of the normalized lithium area over time was conducted, as shown in Fig. 2c, and the same conclusion was confirmed. During the short-term relaxation period after plating, the lithium area decreased, which may indicate the refinement of lithium morphology.

In-situ EIS can decouple various physicochemical processes within the battery across different frequencies, providing evidences for the changes in composition and structure. As shown in Fig. 2d, after lithium plating, the size of the single EIS semi-circle observed in the Nyquist plot became significantly smaller compared to the LiC_6 state, but gradually increased during the relaxation period. The equivalent circuit model (ECM) fitting[41-43] results are shown in Fig. 2e and Supplementary Table 2. Within the short-term (1-2 hours) relaxation after lithium plating, the Ohmic resistance R_0 (reflecting SEI resistance)[44,45] and the interfacial capacitance Y_0 (reflecting the double-layer capacitance)[46,47] both decreased, while in the long-term relaxation, they both increased. These phenomena indicated differences in SEI composition between short and long term relaxation after lithium plating, as well as the reduction in the surface area of the plated lithium, consistent well with the previous conclusions.
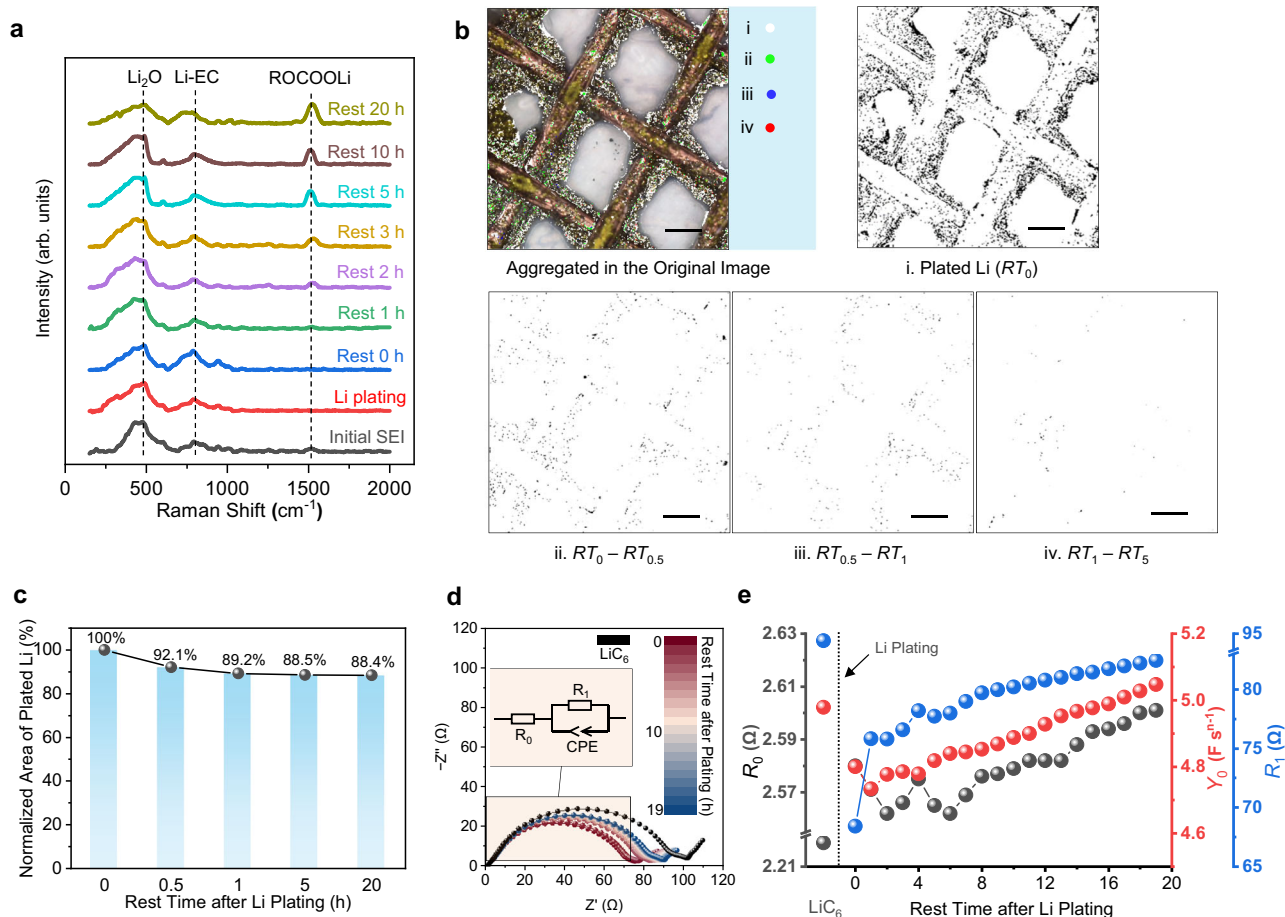
Fig. 2 | In-situ Raman-optical microscopy-EIS analyses during relaxation after lithium plating. a In-situ Raman results. **b** In-situ optical microscopy results after processing, where RT_n represents the area of lithium after n hours resting, and $RT_m - RT_n$ represents the lithium area after m hours minus that after n hours resting. The black bar in each subplot represents 250 μm length. **c** Normalized lithium area over time. **d** EIS measurement results. **e** Equivalent circuit model (ECM) fitting results of EIS.

Ex-situ semi-quantitative analysis

However, due to the focusing changes and resolution limitations, in-situ analyses cannot provide precise quantitative analysis, necessitating the use of additional characterization techniques for a more comprehensive understanding. In this study, we disassembled the cells at various resting times after lithium plating, and conducted semi-quantitative analyses of the SEI composition both along the thickness direction and across time intervals using XPS, TEM and SEM-EDS.

The XPS analysis results for $C\ 1s$, $O\ 1s$ and $F\ 1s$ of 20 hours relaxation after lithium plating are shown in Fig. 3a. We performed experiments at different etching depths (0, 5, 15 and 30 nm, and the value mentioned for each pattern is the depth from the electrode surface) to capture the SEI growth along thickness[48–50]. As the SEI growing after lithium plating (from deeper to shallower layers), the C-C/C-H component gradually increased, accompanied by a decrease in Li_2CO_3, Li_2O and LiF, indicating a transition in the SEI composition from inorganic to organic components. Subsequently, we compared these finding with the elemental composition obtained from the LiC_6 state (Supplementary Fig. 6), as shown in Fig. 3b. The elemental distribution at 30 nm etching of the lithium plated sample closely matched that of the un-etched LiC_6 state, indicating that the newly formed SEI was approximately 30 nm thick, with a surface layer that contained a significantly higher proportion of organic components (rich of C element) compared to the original SEI. High-resolution transmission electron microscopy (HRTEM) and EDS analysis also demonstrate the SEI structure with an inner inorganic layer and an outer organic layer, as detailed in Supplementary Fig. 7-8.

Simultaneously, on the temporal scale, we disassembled the cells with different resting times after lithium plating and conducted SEM-EDS characterization. The elemental composition changes over time are presented in Fig. 3c. Prior to lithium plating, the C content in the negative electrode was the highest among the samples, which could be attributed both to the graphite negative electrode and to the carbonaceous components within the SEI. At 0 hour after lithium plating, the C significantly decreased, while O and F markedly increased, indicating the disruption of the original SEI, and the surface of the plated lithium became relatively enriched in O and F elements. As the relaxation continued, the C content gradually rose while O and F gradually decreased, which represented the progressive formation of an organic SEI. This observation aligns with the aforementioned in-situ Raman and ex-situ XPS results.

Consequently, in terms of chemical evolution, the SEI formed during short-term relaxation after lithium plating is rich in dense and elastic inorganic components. In contrast, long-term relaxation leads to the formation of a fragile organic SEI, and excessively consumes active lithium. This may be one of the primary reasons for the higher capacity retention during short-term relaxation after plating. In recent reports, the formation of this anion-enhanced SEI is attributed to anion migration in the electric field relaxation during the resting period[51].

The mechanism of morphological evolution during relaxation

According to the SEM characterization results shown in Fig. 3d and the statistical analysis of dendrite diameters shown in Supplementary Fig. 9, the lithium dendrites exhibited a trend of being thicker and smoother as relaxation continued. The thickening was likely due to the massive growth of organic SEI, and the smoothing may be a result of morphological changes, consistent with the optical results in Fig. 2b. Therefore, we further investigated the mechanism of morphological changes during the relaxation period after lithium plating by phase-field modeling[23,52,53]. We simulated the growth of lithium dendrites by applying an overpotential, and compared the dendrites morphology, Li^+ concentration field distribution, and liquid-phase potential field distribution at three different stages: 20 seconds before the termination of lithium plating, the termination point, and 20 seconds relaxation after lithium plating, as shown in Fig. 4a.
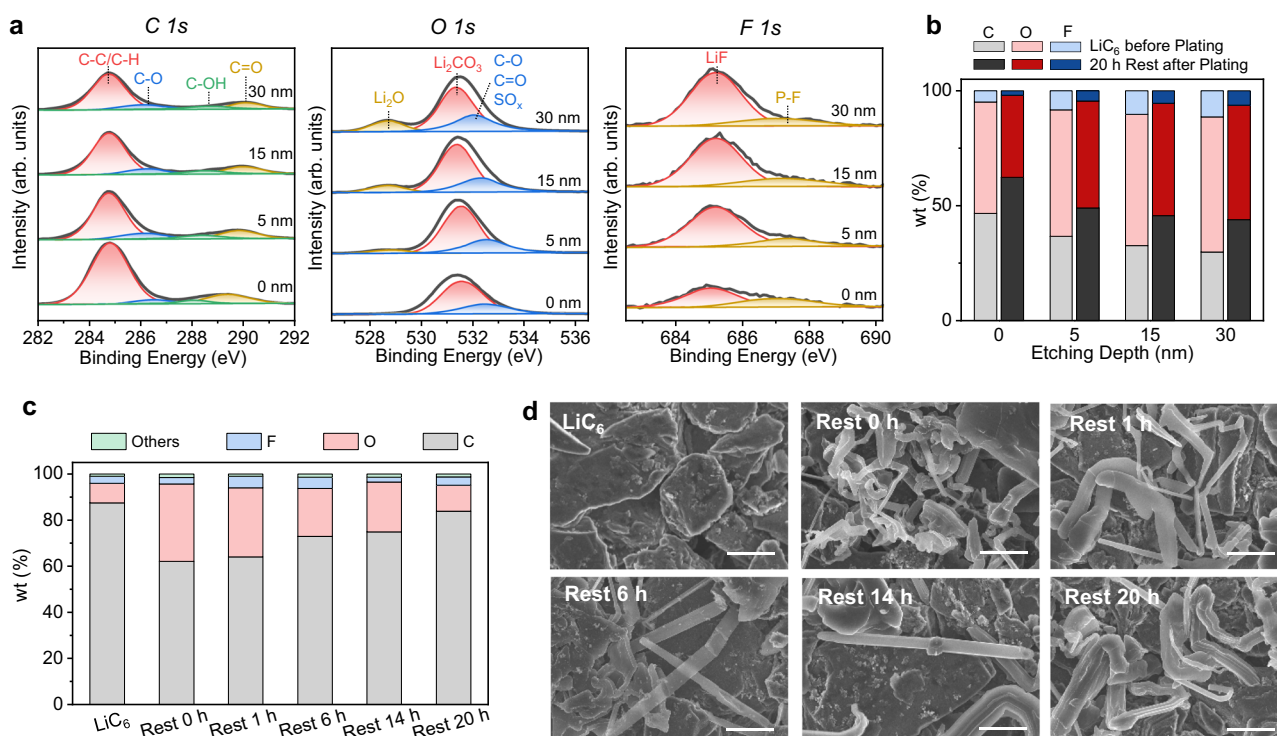
Fig. 3 | Ex-situ characterization results of chemical and structural evolution after lithium plating. a XPS analysis results after 20 hours relaxation. **b** Comparison of elemental composition before and 20 hours after lithium plating. **c** EDS analysis results. **d** SEM characterization results, the white bar in each subplot represents 5 μm length.
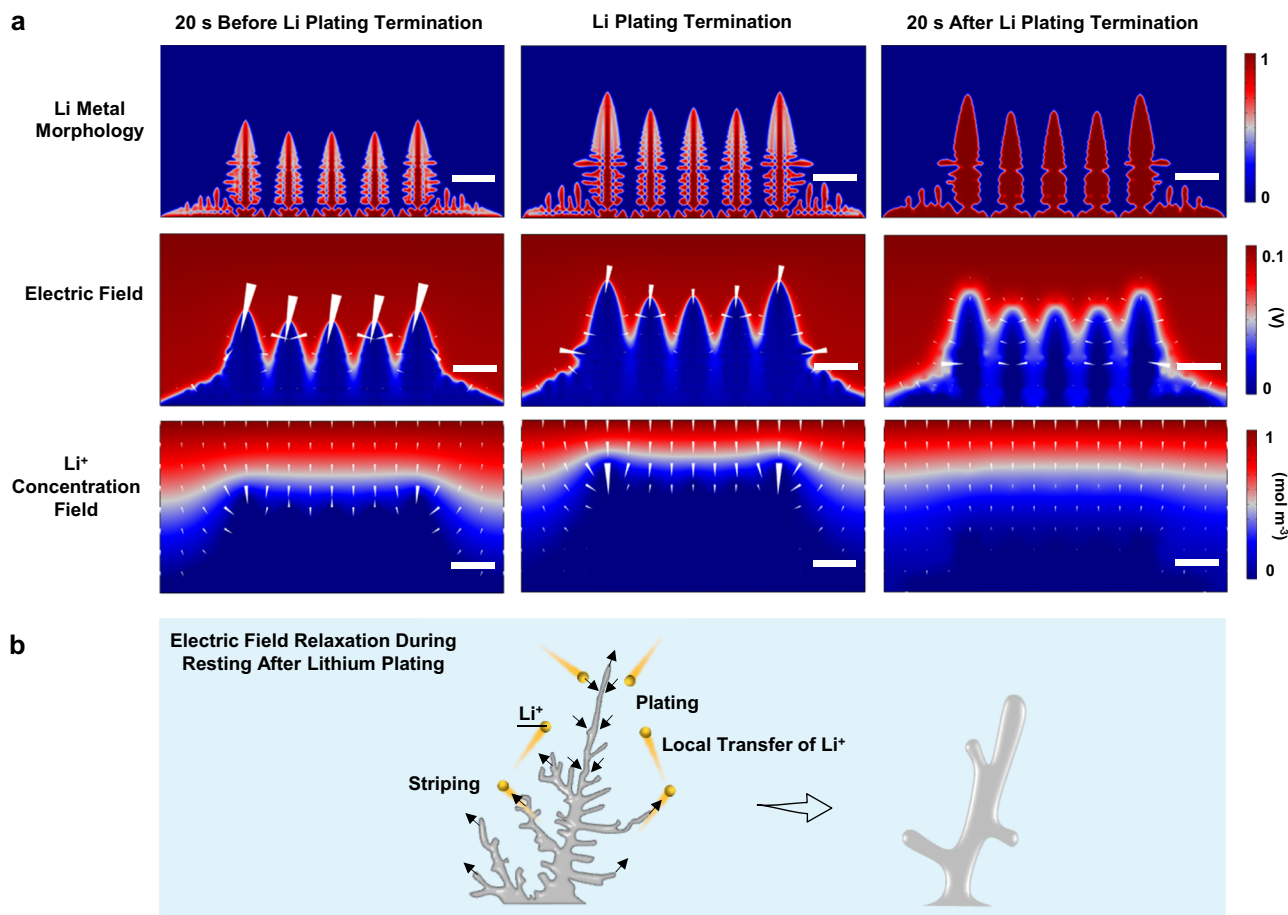
Fig. 4 | The evolution mechanism of plated lithium morphology. a Phase field modeling of different states during lithium plating and relaxation, the white bar in each subplot represents 1 µm length. In the Li metal morphology diagrams, the pure red areas represent the Li metal regions, the pure blue areas represent the electrolyte regions, and the intermediate zone is the transition zone of the phase field variable. The arrows represent the electric field direction and Li$^+$ transport direction, respectively. **b** Schematic diagram of the morphology flattening due to the electric field relaxation during resting.

The deposition of lithium metal exhibited dendritic form. This is driven by the potential field gradient pointing towards the lithium tips, which pumped Li$^+$ to accumulate at the sharp tips, leading to the formation of needle-like dendrites. At the time point when lithium deposition terminated, the electric field still remained concentrated at the dendrite tips. Surprisingly, during the relaxation period after lithium plating, the absence of current and overpotential led to a rapid dissipation of the electric field gradient, which no longer focused on the dendrite tips. As a result, the Li$^+$ concentration gradient at the non-tip regions became higher than that at the tips. This redistribution caused Li$^+$ to locally strip from the tips and plat to the sides, resulting in localized charge transfer, which gradually smoothed and thickened the dendritic structure.

We also conducted simulations and comparisons for traditional immediate stripping regulation after lithium plating, as shown in Supplementary Fig. 10. Similar to the plating process, the electric field gradient and Li$^+$ concentration gradient was also concentrated at the tips during the discharging process, with Li$^+$ continuously stripped-off and no local-transfer occurred. This enhanced the propensity of lithium metal stripping at the tips, and caused the thinner regions to become even thinner, which eventually led to fracture of the tips, resulting in the formation of isolated lithium[53].

In contrast to the conventional method of immediate discharge the negative electrode after lithium plating, and activate isolated lithium by post-discharge resting, the short-term relaxation strategy directly after lithium plating allows for the relaxation of electric and concentration fields, which induces a redistribution of lithium metal

from the dendrite tips to the sides (as illustrated in Fig. 4b), smoothing the dendrite structures and reducing the formation of isolated lithium.

Lithium plating manipulation based on electric field relaxation

In short summary, this study identifies two key factors contributing to the capacity recovery during short-term relaxation after lithium plating: (1) the formation of a thin, robust and inorganic-rich SEI, and (2) the smoothing of lithium dendrites, which helps to reduce dead lithium formation. Both effects are attributed to the relaxation of the electric field during the short-term relaxation period immediately after lithium plating. The schematic of this process is presented in Fig. 5a.

Finally, we accessed the practical application of our findings. We conducted fast charging experiments using commercial Gr||LiFePO$_4$ batteries under 3 C-rate (2.7 A), and compared the capacity degradation for 100 cycles across different test groups. In each group, the cells were rested for a hours after charging and for b hours after discharging (Supplementary Fig. 11 and Supplementary Table 3). The unregulated cells ($a = 0$, $b = 0$) experienced rapid capacity decay, losing 20% capacity after 100 cycles (Supplementary Fig. 12). SEM characterization revealed substantial lithium plating on the negative electrode (Supplementary Fig. 13). The degradation results of the manipulated groups are shown in Fig. 5b. Compared to 10-hour resting after lithium plating ($a = 10$, $b = 0$), 10-hour resting at discharged state ($a = 0$, $b = 10$) proposed in ref. 27 showed batter capacity retention. Nonetheless, it was still less effective than the short-term relaxation following lithium plating ($a = 2$, $b = 8$). Additionally, our proposed method ($a = 1$, $b = 1$) achieved an enhancement in capacity retention from 80% to 95% over
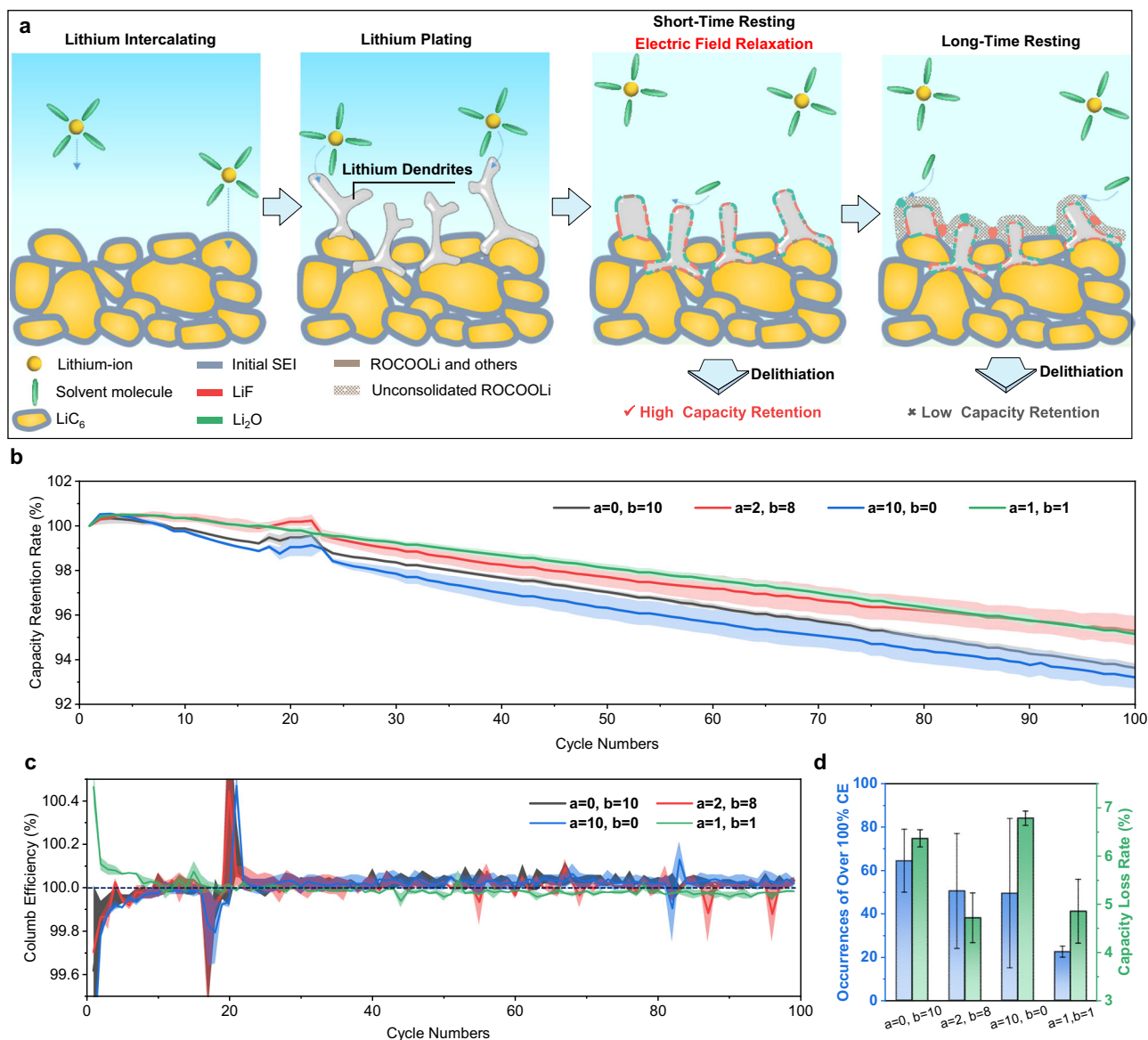
Fig. 5 | Lithium plating manipulation based on short-term relaxation.
a Schematic diagram of manipulation mechanism. **b** Degradation of commercial Gr||LFP batteries under 3 C-rate lithium plating fast-charging condition and different manipulation protocols. **c** CE of the batteries in **b**, and **d** Comparison of CE and capacity loss under different manipulation conditions. Two cells were tested per group for statistical representation, and the shading represents the range between the maximum and minimum values.

100 rapid-charging cycles, in contrast to the absence of any regulation. Compared to the state-of-the-art discharging-resting method ($a = 0$, $b = 10$), it reduced capacity loss by 23.8% while shortening the regulation time by 80%. Moreover, the short-term relaxation after fast charging aligns more closely with typical user behaviors, thus offering practical value.

We then analyzed the voltage profiles during relaxation after fast charging and lithium plating, thereby substantiating the scientific basis for a 1-hour relaxation period (which was the time constant of the electric field relaxation process) as the optimal solution, as shown in Supplementary Fig. 14. We also compared the CE under these regulation conditions, as shown in Fig. 5c. Surprisingly, the condition with the highest capacity retention ($a = 1$, $b = 1$) exhibited the lowest CE, remaining below 100% for most cycles. In contrast, the CE for the other three conditions stayed around or above 100%. Furthermore, we analyzed the number of cycles where the CE exceeded 100% over 100 cycles, and examined its correlation with the capacity loss rate after 100 cycles, as shown in Fig. 5d. The results showed no significant

correlation between the two parameters, which is contrary to previous perceptions[54,55]. The discharging-resting group ($a = 0$, $b = 10$) exhibited the highest occurrences of CE exceeding 100%, likely due to the reactivation of dead lithium during the relaxation period[27]. However, this group also experienced a higher degradation rate, which can be attributed to the increased formation of dead lithium from immediate discharge after lithium plating. The underlying cause of this phenomenon is that the conventional CE calculation method only accounts for the capacity retention within a single cycle[56]. To capture the capacity retention across multiple cycles, a distinct method of calculation is discussed in Supplementary Fig. 15-16. This further supported that short-term relaxation after lithium plating reduced the formation of dead lithium at its source, leading to a higher capacity retention.

Discussion

In this study, we found the counterintuitive phenomenon that short-term relaxation after lithium dendrites formation led to the highest

capacity retention. We then conducted an in-depth investigation into the chemical and physical changes occurring during the relaxation period after lithium plating to elucidate the underlying mechanisms of the process. Utilizing in-situ Raman spectroscopy-optical microscopy-EIS, we analyzed the changes in lithium dendrites' composition and morphology during relaxation. In the short-term relaxation, an SEI rich in inorganic components was formed, accompanied by a reduction in the metallic lithium surface area. While long-term relaxation led to the predominant formation of organic SEI, with little change in the morphology. Furthermore, through ex-situ XRD, TEM and SEM-EDS analyses, we semi-quantitatively validated the formation process of SEI structure from both thickness and temporal perspectives, and confirmed the gradual transition of composition from inorganic to organic phases. Additionally, based on phase-field modeling, we analyzed the morphological evolution from sharp to smooth during the relaxation period, which is driven by the localized transfer of Li^+ from the dendrite tips to the sides. Therefore, the competitive relationship between morphological optimization and SEI film deterioration during short-term relaxation after lithium plating result in the highest capacity retention. The common underlying mechanism for both changes is the relaxation of the electric field. Finally, we discussed the practical implication of our findings. In commercial $LiFePO_4$ batteries, our short-term resting strategy after fast charging increased the capacity retention rate from 80% to 95% after 100 cycles at 3 C-rate (1 A), and compared to the state-of-the-art discharging-resting regulation protocol, our method achieved an 80% reduction in time, and reduced capacity loss by 23.8%. We also observed that capacity loss was unrelated to Coulomb Efficiency, for the CE under the highest capacity retention protocol was the lowest.

This research demonstrated the theoretical and practical feasibility of simultaneously suppressing the formation of detrimental SEI and dead lithium at the source by regulation method, which can guide further studies on the safe and long-life manipulation for lithium dendrites of lithium-based batteries, holding significant potential for practical applications on fast charging and low-temperature charging.

Methods

Li||Gr cell

In the research on capacity retention under different lithium plating and manipulation conditions, we used 2032-type coin cells employing graphite negative electrode (5.8 mg cm^{-2}, 340 mAh g^{-1}, Canrd), high-purity Li foil (200 μm thick, 99.9%, Φ14mm, Xiamen TOB New Energy Co., Ltd.), 2325-type PE/PP/PP separator (39% porosity, 25μm, purchased from Celgard), and 20 μL electrolyte (1 mol L^{-1} LiPF$_6$ in 1:1:1 ethylene carbonate (EC)/ ethyl methyl carbonate (EMC)/ dimethyl carbonate (DMC) and 0.5% w/w vinylene carbonate (VC), Canrd). The metallic lithium electrodes and electrolyte were stored in an argon (Ar)-filled glovebox (25 °C, with water and oxygen levels below 0.01 ppm) for no more than one month prior to cell assembly. The separator was stored in a vacuum drying oven at 60 °C for no more than half a year. We punched the Gr electrode and separator into discs with diameters of 12 mm and 19 mm, respectively, and then assemble the coin cells inside the Ar glove box. We used a 2035-type coin cell assembly (stainless-steel positive and negative shells with a diameter of 20 mm and a thickness of 3.5 mm, a stainless-steel washer with a thickness of 0.5 mm and a diameter of 12 mm, and a matching stainless-steel spring, all purchased from Canrd) for assembly, with an assembly pressure of 800 kg. All of the cells were tested after 20 hours electrode soaking process.

Raman spectrometer and microscopy

Raman spectroscopy was performed with a SENTERRA II microscope from Bruker, using a 785 nm laser at 25 mW power. A 50x objective lens focused the laser, and spectra were collected with a 20-second exposure and five accumulations. The aperture was set at 15×1000 μm, achieving a spectral resolution exceeding 4 cm^{-1} for precise vibrational mode identification. Data analysis, including normalization based on the total area[32], was conducted using Matlab R2018b, aiding in the identification and quantification of peaks by their wavenumber and intensity. The testing sample was an in-situ optical cell, with charging and discharging performed using CT3004A battery tester from LANHE.

In-situ optical cell assembly

Compared to conventional coin cells, there are two improvements: (1) Mesh-type Gr negative electrode, we mixed graphite, PVDF, Super P, and N-methyl-2-pyrrolidone (all purchased from Celgard) in 9:0.5:0.5:25 ratio to produce the slurry. The slurry was prepared by mixing six times at 1800 r min^{-1} for 3 minutes each using a planetary centrifugal defoaming mixer (SZKEJING) under 25 °C. Then, a 40-mesh, 200 μm thick copper mesh was cut into 12 mm diameter discs, dipped into the slurry, and baked at 80 °C for 10 hours to prepare the mesh-type Gr negative electrode. The areal density of the prepared mesh electrode was 7 mg cm^{-2}, and the total thickness was 220 μm. (2) Positive electrode shell, a 5 mm diameter hole was drilled in the center of the positive electrode shell, then a 500 μm thick, 10 mm diameter sapphire glass was placed on top and sealed with adhesive (Kafuter). After curing, a layer of copper paint was sprayed, and a sticker was used to retain a 5 mm diameter transparent window. The lithium foil, separator, electrolyte, and cell assembly used here are exactly the same as those used in the aforementioned Li||Gr cell. The detailed manufacturing processes of the in-situ optical cell are shown in Supplementary Fig. 2.

Optical image to RGB colourmap processing

The images were decomposed into RGB channels using the method provided in ref. 27, and the lithium plating areas were subsequently extracted. First, we located the MP4 video at the specific time points in Fig. 2, and converted them into PNG images. Then, the images were decomposed into new images corresponding to the intensity of red, green, and blue in the raw images. To distinguish golden LiC_6 and purplish-red copper (mainly composed of red and green) from the gray metallic lithium (with similar proportions of red, green, and blue), we used the blue channel to separate the lithium areas. By subtracting the blue channel image before the start of lithium plating from that after the lithium plating, the area of metallic lithium was obtained. However, due to the subtle changes in the brightness of the separator area and the generation and movement of some bubbles, some areas may be mistakenly identified as lithium metal. To correct this, we manually adjusted the threshold to separate the separator area from the Gr mesh-lithium metal area, and manually removed the areas of bubbles.

Battery cycling tests

For the cycling of coin cells, we employed CT3004A battery tester from LANHE, while for the pouch cells, we used CT-4008 battery tester from NEWARE. The testing procedures followed specially designed protocols, which are detailed in the accompanying text. A BTT-series temperature chamber from GDBELL Co., Ltd. was utilized to maintain a stable environment at 25 °C ± 1 °C. The data was collected at a sampling rate of 1 Hz.

As for the protocols that trigger lithium plating, we used overcharging to trigger lithium plating on coin cells. By precisely controlling the overcharge capacity, we can accurately control the amount of lithium plating while eliminating the impact of inconsistencies between different cells. And for the pouch cells, we employed fast charging to trigger lithium plating. This method is closer to real-world scenarios, providing valuable insights for our proposed approach to be

used in practical applications. By analyzing the experimental results, we are fully confident that the morphology and transformation principles of lithium plating induced by overcharging and fast charging are similar.

EIS measurement and data processing

EIS measurements were conducted using an Autolab modular system (PGSTAT302N, Metrohm Co., Ltd.) in potentiostatic mode, the amplitude perturbation was 10 mV. The sweep frequency for all cells were 10^6 to 10^{-2} Hz, with 10 data points per decade of frequency, encompassing the charge-transfer processes outlined in the text. Also, BTT-series temperature chamber from GDBELL Co., Ltd. was utilized to maintain a stable environment at 25 °C ± 1 °C. The ZVIEW software was utilized to fit the parameters of the equivalent circuit model[23].

XPS

XPS is a widely adopted technique for analyzing SEI structures[57,58]. In this study, XPS measurements were conducted utilizing the ESCALAB Xi+ (Thermofisher Scientific) with a monochromatized Al Kα X-ray source. The Li||Gr cells were disassembled in an Ar glovebox at 25 °C, with Gr negative electrode soaked in 50 mL DMC for 4 hours to thoroughly remove residual electrolyte. Then the electrode was placed in the glovebox for 10 hours to ensure complete drying. Samples were vacuum-transferred to the XPS measurement instrument to minimize air exposure, maintaining a chamber pressure of 10^{-7} Pa during testing and data collection. Neutralization was ensured with electron and ion guns. The Avantage software was used for XPS analysis, with the C 1s peak at 284.5 eV as a reference. SEI atomic ratios were calculated from survey scans at 224 eV pass energy.

HRTEM-EDS

HRTEM analyses were performed using a 200 kV Thermo Fisher Talos F200S field-emission transmission electron microscope. The elemental composition and distribution within the area of interest were characterized via EDS mapping. Digital Micrograph software was employed for FFT transformation of TEM images and lattice parameter measurements, which facilitated the identification of crystal structure and type. The cell disassembly, electrode cleaning, drying, and transfer procedures were consistent with those mentioned in the XPS section.

SEM-EDS

The morphology of plated lithium on Gr negative electrodes was characterized using a Merlin high-resolution SEM (Carl Zeiss AG). In an Ar-filled glovebox, coin and pouch cells were disassembled to isolate lithium-plated graphite negative electrodes. Electrode terminals were cleaned in 50 mL DMC for 4 hours to eliminate Li$^+$ salts and impurities, then dried for 10 hours and cut into 5 mm^2 pieces for SEM analysis in an Ar transfer chamber. The sample was placed in an Ar-filled transfer chamber and moved to the SEM equipment without any exposure to air throughout the process.

Phase-field modeling

By employing COMSOL Multiphysics v.6.1, we modeled the phase-field dynamics within an 8 μm × 4 μm electrolyte domain, filled with a 1 mol L^{-1} LiPF6 solution in EC/EMC/DMC (1:1:1). A time-dependent solver was used, with a 0.1 s calculation step. The phase field parameter ξ began at 0, with five lithium plating seeds, each set to ξ = 1, evenly distributed at the domain's base. By manipulating electric field boundary conditions, we simulated the battery's charge, rest, and discharge cycles. Detailed model parameters are provided in the supplementary files in Supplementary Table 4-5.

Commercial Gr||LFP pouch cell

To validate the effectiveness of the lithium plating manipulation methods in the study, we conducted experiments using a commercially available 900 mAh LFP pouch cell from UFine, China, with a rated voltage of 3.2 V and a rated charging rate of 0.5 C. At a charging rate of 3 C (2.7 A), lithium plating was induced, thereby confirming the efficacy of our control strategy for manipulating lithium plating.

It should be noted that the capacity recovery observed in the black, red, and blue curves around the 20th cycle in Fig. 5b is actually due to a period of maintenance and power outage in the laboratory, which led to an increase in ambient temperature and, consequently, an increase in battery capacity. This external condition change had minimal impact on the overall capacity fade trend.

Calculation of Coulomb Efficiency (CE)

The traditional CE (also reported in Fig. 5c) was calculated as the ratio of discharge capacity divided by the charge capacity in the preceding charge cycle, independently of whether a cell/battery was assembled in a charged or discharged state. In Fig. 5d, we introduced an uncommon calculation method for Coulombic efficiency, defined as the ratio of the charge capacity at the current cycle to the charge capacity at the previous cycle. Our analysis indicated that this approach can more accurately reflect the trend of battery cycle decay.

Statistical information

The error bars in Fig. 1c represent the standard deviation, and each experimental group was tested three times for reproducibility. The error lines in Fig. 5b–d represent the maximum and minimum values of the experimental results, and each experimental group includes two repeated experiments. The data presented in the manuscript's plots represent a statistical analysis of all the cells tested for the electrochemical experiments.

Data availability

The datasets generated and analyzed in this work are included in this article and Supplementary Information. Source data are provided with this paper.

References

1. He, M. N. et al. Industry needs for practical lithium-metal battery designs in electric vehicles. *Nat. Energy* https://doi.org/10.1038/s41560-024-01624-5 (2024).
2. Cui, Y. & Ye, Y. S. Porous current collector for fast-charging lithium-ion batteries. *Nat. Energy* **9**, 639–640 (2024).
3. Wang, C. Y. et al. Fast charging of energy-dense lithium-ion batteries. *Nature* **611**, 485 (2022).
4. Zeng, Y. et al. Extreme fast charging of commercial Li-ion batteries via combined thermal switching and self-heating approaches. *Nat. Commun.* **14**, https://doi.org/10.1038/s41467-023-38823-9 (2023).
5. Lu, L.-L. et al. Extremely fast-charging lithium ion battery enabled by dual-gradient structure design. *Science Advances* **8**, https://doi.org/10.1126/sciadv.abm6624 (2022).
6. Tu, S. et al. Fast-charging capability of graphite-based lithium-ion batteries enabled by Li3P-based crystalline solid-electrolyte interphase. *Nat. Energy* **8**, 1365–1374 (2023).
7. Xu, L., Lei, S., Srinivasan, D. & Song, Z. Can retired lithium-ion batteries be a game changer in fast charging stations? *eTransportation* **18**, https://doi.org/10.1016/j.etran.2023.100297 (2023).
8. Konz, Z. M. et al. High-throughput Li plating quantification for fast-charging battery design. *Nat. Energy* **8**, 450–461 (2023).
9. Tian, Y. et al. Reversible lithium plating on working anodes enhances fast charging capability in low-temperature lithium-ion batteries. *Energy Storage Mater.* **56**, 412–423 (2023).
10. Huang, W. et al. Onboard early detection and mitigation of lithium plating in fast-charging batteries. *Nat. Commun.* **13**, https://doi.org/10.1038/s41467-022-33486-4 (2022).

11. Jin, C. et al. Rejuvenating dead lithium supply in lithium metal anodes by iodine redox. *Nat. Energy* **6**, 378–387 (2021).

12. Zheng, M. et al. Voltage-induced bromide redox enables capacity restoration of fast-charging batteries. *Adv. Mater.* https://doi.org/10.1002/adma.202414207 (2024).

13. Lin, D. et al. Fast galvanic lithium corrosion involving a Kirkendall-type mechanism. *Nat. Chem.* **11**, 382–389 (2019).

14. Boyle, D. T. et al. Corrosion of lithium metal anodes during calendar ageing and its microscopic origins. *Nat. Energy* **6**, 487–494 (2021).

15. Merrill, L. C., Rosenberg, S. G., Jungjohann, K. L. & Harrison, K. L. Uncovering the relationship between aging and cycling on lithium metal battery self-discharge. *Acs Appl. Energy Mater.* **4**, 7589–7598 (2021).

16. Fang, C. C. et al. Quantifying inactive lithium in lithium metal batteries. *Nature* **572**, 511 (2019).

17. Lin, X., Shen, Y., Yu, Y. & Huang, Y. In Situ NMR Verification for Stacking Pressure-Induced Lithium Deposition and Dead Lithium in Anode-Free Lithium Metal Batteries. *Advanced Energy Materials* **14** https://doi.org/10.1002/aenm.202303918 (2024).

18. Vishnugopi, B. S. & Mukherjee, P. P. "Dead"lithium or back from the "dead"? *Joule* **6**, 291–293 (2022).

19. Liu, F. et al. Dynamic spatial progression of isolated lithium during battery operations. *Nature* **600**, 659 (2021).

20. Liao, G. F., Zhou, B. X. & Fang, B. Z. Reconnection of isolated lithium through fast discharge. *Trends Chem.* **4**, 855–856 (2022).

21. Merrill, L. C. et al. Role of coatings as artificial solid electrolyte interphases on lithium metal self-discharge. *J. Phys. Chem. C.* **126**, 17490–17501 (2022).

22. Reisecker, V. et al. Effect of pulse-current-based protocols on the lithium dendrite formation and evolution in all-solid-state batteries. *Nat. Commun.* **14**, 2432 (2023).

23. Mao, S. et al. In situ evaluation and manipulation of lithium plating morphology enabling safe and long-life lithium-ion batteries. *Infomat* https://doi.org/10.1002/inf2.12612 (2024).

24. Fuchs, T. et al. Current-dependent lithium metal growth modes in "anode-free" solid-state batteries at the Cu|LLZO interface. *Adv. Energy Mater.* **13**, https://doi.org/10.1002/aenm.202203174 (2023).

25. Yang, Y. et al. Capacity recovery by transient voltage pulse in silicon-anode batteries. *Science* **386**, 322–327 (2024).

26. Jin, C. & Tao, X. Electric pulses rejuvenate batteries Dielectrophoresis allows "dead" material to recover its activity. *Science* **386**, 276–276 (2024).

27. Zhang, W. et al. Recovery of isolated lithium through discharged state calendar ageing. *Nature* **626**, https://doi.org/10.1038/s41586-023-06992-8 (2024).

28. Lin, X. K., Khosravinia, K., Hu, X. S., Li, J. & Lu, W. Lithium plating mechanism, detection, and mitigation in lithium-ion batteries. *Prog. Energ. Combust.* **87**, 30 (2021).

29. Mei, W. X., Jiang, L. H., Liang, C., Sun, J. H. & Wang, Q. S. Understanding of Li-plating on graphite electrode: detection, quantification and mechanism revelation. *Energy Storage Mater.* **41**, 209–221 (2021).

30. Yuan, X. T., Liu, B., Mecklenburg, M. & Li, Y. Z. Ultrafast deposition of faceted lithium polyhedra by outpacing SEI formation. *Nature* **620**, 86 (2023).

31. Wang, Y., Zhang, X., Li, K., Zhao, G. & Chen, Z. Perspectives and challenges for future lithium-ion battery control and management. *Etransportation* **18**, https://doi.org/10.1016/j.etran.2023.100260 (2023).

32. Cabañero, M. A., Hagen, M. & Quiroga-González, E. In-operando Raman study of lithium plating on graphite electrodes of lithium ion batteries. *Electrochimica Acta* **374**, 137487 (2021).

33. Liu, D. et al. Review of recent development of in situ/operando characterization techniques for lithium battery research. *Adv. Mater.* **31**, 1806620 (2019).

34. Tripathi, A. M., Su, W.-N. & Hwang, B. J. In situ analytical techniques for battery interface analysis. *Chem. Soc. Rev.* **47**, 736–851 (2018).

35. Kong, F. et al. In situ studies of SEI formation. *J. Power Sources* **97-8**, 58–66 (2001).

36. Naudin, C. et al. Characterization of the lithium surface by infrared and Raman spectroscopies. *J. Power Sources* **124**, 518–525 (2003).

37. Tu, S. B. et al. Fast-charging capability of graphite-based lithium-ion batteries enabled by LiP-based crystalline solid-electrolyte interphase. *Nat. Energy* **8**, 1365–1374 (2023).

38. Oyakhire, S. T. et al. Correlating the formation protocols of solid electrolyte interphases with practical performance metrics in lithium metal batteries. *Acs Energy Lett.* **8**, 869–877 (2023).

39. Guo, J. et al. Unravelling the mechanism of pulse current charging for enhancing the stability of commercial LiNiMnCoO/graphite lithium-ion batteries. *Adv. Energy Mater.* **14**, https://doi.org/10.1002/aenm.202400190 (2024).

40. Jagger, B. & Pasta, M. Solid electrolyte interphases in lithium metal batteries. *Joule* **7**, 2228–2244 (2023).

41. Zhang, Y. et al. Identifying degradation patterns of lithium ion batteries from impedance spectroscopy using machine learning. *Nat. Commun.* **11**, https://doi.org/10.1038/s41467-020-15235-7 (2020).

42. Petzl, M., Kasper, M. & Danzer, M. A. Lithium plating in a commercial lithium-ion battery A low-temperature aging study. *J. Power Sources* **275**, 799–807 (2015).

43. Pastor-Fernandez, C., Uddin, K., Chouchelamane, G. H., Widanage, W. D. & Marco, J. A Comparison between electrochemical impedance spectroscopy and incremental capacity-differential voltage as Li-ion diagnostic techniques to identify and quantify the effects of degradation modes within battery management systems. *J. Power Sources* **360**, 301–318 (2017).

44. Zhao, J. & Abu Qahouq, J. A. Modeling and validation for performance analysis and impedance spectroscopy characterization of lithium-ion batteries. *Next Energy* **5**, https://doi.org/10.1016/j.nxener.2024.100153 (2024).

45. Meddings, N. et al. Application of electrochemical impedance spectroscopy to commercial Li-ion cells: a review. *Journal of Power Sources* **480**, https://doi.org/10.1016/j.jpowsour.2020.228742 (2020).

46. Xu, L. et al. Operando quantified lithium plating determination enabled by dynamic capacitance measurement in working Li-ion batteries. *Angew Chem Int Edit* https://doi.org/10.1002/anie.202210365 (2022).

47. Xu, L. et al. In Situ Li-plating diagnosis for fast-charging Li-ion batteries enabled by relaxation-time detection. *Advanced Materials* **35**, https://doi.org/10.1002/adma.202301881 (2023).

48. Zhu, D. W. et al. Boron-doped electrolytes as interfacial modifiers for high-rate stable lithium metal batteries. *Adv Funct. Mater.* **33**, 2213822 (2023).

49. Capone, F. G. et al. observation of the dynamic SEI formation on a carbonaceous electrode by near-ambient pressure XPS. *Energ. Environ. Sci.* **17**, 1509–1519 (2024).

50. Heiskanen, S. K., Kim, J. & Lucht, B. L. Generation and evolution of the solid electrolyte interphase of lithium-ion batteries. *Joule* **3**, 2322–2333 (2019).

51. Yuan, X. et al. Engineering battery corrosion films by tuning electrical double layer composition. *Joule* https://doi.org/10.1016/j.joule.2024.07.011 (2024).

52. Chen, L. et al. Modulation of dendritic patterns during electrodeposition: a nonlinear phase-field model. *J. Power Sources* **300**, 376–385 (2015).

53. Zhang, R. et al. Dead lithium formation in lithium metal batteries: a phase field model. *J. Energy Chem.* **71**, 29–35 (2022).

54. Hobold, G. M. et al. Moving beyond 99.9% Coulombic efficiency for lithium anodes in liquid electrolytes. *Nat. Energy* **6**, 951–960 (2021).

55. Xiao, J. et al. Understanding and applying coulombic efficiency in lithium metal batteries. *Nat. Energy* **5**, 561–568 (2020).

56. Li, J.-L. et al. Understanding and regulating the mechanical stability of solid electrolyte interphase in batteries. *Adv. Energy Mater*. https://doi.org/10.1002/aenm.202403845 (2024).

57. Gao, A. et al. Interphase design enabling stable cycling of all-solid-state lithium metal batteries by in-situ X-ray photoelectron spectroscopy lithium metal sputtering. *Journal of Power Sources* **602**, https://doi.org/10.1016/j.jpowsour.2024.234299 (2024).

58. Liang, Y. et al. In situ XPS investigation of the SEI formed on LGPS and LAGP with metallic lithium. *Chem. Commun.* **60**, 12597–12600 (2024).

Acknowledgements

Author contributions

X.H. conceived the idea and supervised the research. S.M. conducted the experiments, built the models, analyzed the experiment results and wrote the manuscript. Y.W., Y.L., L.L., and M.O. discussed the results and commented on the manuscript. D.W., Y.S., Y.Z., X.F., and J.H. provided the experimental equipment and guided the equipment usage.

Competing interests

The authors declare no competing interests.

Additional information

Correspondence and requests for materials should be addressed to Xuebing Han, Shuoyuan Mao, Yu Wang, Yuejiu Zheng or Minggao Ouyang.

Peer review information *Nature Communications* thanks Zheng Liang, Yujing Liu, and the other, anonymous, reviewer(s) for their contribution to the peer review of this work. A peer review file is available.

Reprints and permissions information is available at http://www.nature.com/reprints

Publisher's note Springer Nature remains neutral with regard to jurisdictional claims in published maps and institutional affiliations.